Plasma Actuation and Bispectral Mode Decomposition of Supersonic Twin-Rectangular Jet Flow

Brandon C. Y. Yeung* and Oliver T. Schmidt†
University of California San Diego, La Jolla, California 92093

Large-eddy simulations (LES) of a Mach 1.5, nominally ideally-expanded, twin-rectangular jet are performed, with and without forcing. The numerical implementation of the periodic forcing is based on companion experiments at Ohio State University that utilize localized arc filament plasma actuators (LAFPA) to control twin-jet coupling and influence jet screech. In the forced jet LES, twelve independently-controlled energy sources, which model LAFPAs, generate bursts of thermal and pressure perturbations in a pattern that is symmetric about the major and minor axes of the jet, or symmetric-symmetric for short. For rigorous statistical analysis, the natural and forced jet data are decomposed into their D_2-symmetry components, which are either symmetric or antisymmetric about the major and/or minor axes. To identify large-scale structures involved in triadic interactions, bispectral mode decomposition (BMD) is applied to the forced case, leading to a complex mode bispectrum and three-dimensional BMD modes for each D_2 symmetry component (auto-BMD) or set of components (cross-BMD). The BMD analyses reveal dominant triadic interactions between symmetric-symmetric modes, associated with the forcing, and between antisymmetric-symmetric modes, associated with the natural screech tone. Both classes of symmetry-self interactions generate superharmonics and mean flow distortions that are symmetric-symmetric. In contrast, symmetry-cross interactions between the symmetric-symmetric forcing and antisymmetric-symmetric screech form superharmonics and mean flow deformations that are antisymmetric-symmetric. Summed mode spectra, obtained from the average along each diagonal of the BMD bispectra, suggest that under the present forcing, consistent symmetry (i.e., either both symmetric, or both antisymmetric) about the minor axis is a prerequisite for two modes to interact quadratically.

Nomenclature

c	=	speed of sound
D_e	=	equivalent nozzle diameter $1.6h$
D_n	=	dihedral group with n mirror symmetries
f	=	frequency
h	=	nozzle height
k	=	actuator temporal signal
L	=	actuator length
l, m	=	actuator spatial supports
M	=	Mach number
$N_{(\cdot)}$	=	number of $(\cdot)$
P	=	actuator power
p	=	pressure
$\mathbf{q}$	=	state vector
Re	=	Reynolds number
r	=	radial coordinate
r_0	=	actuator radius
S	=	energy source
St	=	Strouhal number fD_e/U_j
T	=	temperature
t	=	time

*Ph.D. Student, Department of Mechanical and Aerospace Engineering, Student Member AIAA.
†Associate Professor, Department of Mechanical and Aerospace Engineering, Senior Member AIAA.

$t_{\text{on}}, t_{\text{off}}$ = time instants when actuator switches on or off
t_r = actuator rise time
U = mean streamwise velocity
x, y, z = Cartesian coordinates
γ = adiabatic constant c_p/c_V
Λ = BMD summed mode spectrum
λ = BMD complex mode bispectrum
μ = dynamic viscosity
$\boldsymbol{\phi}$ = BMD mode
ρ = density
σ = actuator sharpness parameter
τ = forcing period

Subscript

a = acoustic property
blk = blocks
cv = control volumes
d = design
j = fully-expanded nozzle exit property
max, min = maximum, minimum
ovlp = overlap
t = stagnation property
∞ = ambient property

Superscript

$\bar{(\cdot)}$ = long-time mean
$\hat{(\cdot)}$ = Fourier transform
$(\cdot)'$ = fluctuating

I. Introduction

The control of turbulent jets with the aim of noise reduction has been investigated using a range of passive devices, including chevrons [1–3] and steady microjet injections [4]. These studies have achieved modest noise reduction—usually at low frequencies—but have yet to reveal a unified theory of the mechanisms that underlie the observed reduction. The lack of such a theory is one factor that impedes the progress towards systematic strategies for robust jet noise reduction.

In addition to passive means of flow control, active devices are also the subject of significant ongoing research [5]. While many classes of active devices, including plasma actuators, possess effective control authority in low-speed flows, the control of high-Reynolds number jets relevant to practical engineering applications requires large-amplitude, high-bandwidth forcing [5]. These design requirements are the basis for localized arc filament plasma actuators (LAFPA), developed by Samimy et al. [6]. LAFPAs produce intense localized thermal perturbations and shocks through arc discharge. First experimentally demonstrated in axisymmetric high-subsonic and supersonic jets [6], LAFPAs have received recent attention as flow control devices in military-style nozzles [7, 8]. In a series of companion experiments, Samimy et al. [8] at Ohio State University (OSU) explored the use of LAFPAs to influence the coupling and noise profile of a twin-rectangular supersonic jet, under design and off-design operating conditions. Numerically investigating LAFPA-based control of the same jet forms the subject of this paper.

Of particular interest is the control of jet screech. Powell [9] accompanied his discovery of this intense, spectrally discrete supersonic jet noise with a proposal for its origin: resonance arising from shock-shear layer interaction. This explanation has largely withstood the scrutiny of later research, even if details concerning the precise resonant mechanisms have evolved. It is generally accepted that the screech feedback loop is energized by downstream-propagating Kelvin-Helmholtz (KH) instability waves, which extract energy from the mean flow [10]. The upstream-propagating waves that close the loop, however, are less well-understood, though a consensus is emerging that they are more likely to be neutral acoustic modes with support inside the jet [11] than freestream acoustic modes, at least for an axisymmetric jet. A twin-rectangular jet introduces additional complexities. First, the screech loop of one jet may be receptive to

perturbations originating from its twin [12]. Second, due to its biconical nozzles, the jet contains shock cells and emits screech, even in the nominally ideally-expanded condition under consideration in this paper. Modeling and mitigating the noise emission of a twin-rectangular jet thus remain challenging tasks.

Our goal is therefore twofold: to demonstrate the control authority of LAFPAs in the OSU jet using high-fidelity large-eddy simulations (LES), and to contribute fundamental insights into twin-rectangular jet physics that will support future noise reduction strategies in military-style jets. Building on recent simulations by Brès et al. [13, 14] and Yeung et al. [15] of the natural jet, we numerically model the rapid heating induced by LAFPAs as observed in the laboratory. LAFPA modeling began with Utkin et al. [16], who incorporated a one-dimensional plasma model into the axisymmetric Navier-Stokes equations. This one-dimensional model was extended to two dimensions by Kleinman et al. [17] for a direct numerical simulation of the near-nozzle lip region of a forced axisymmetric jet. The model of Utkin et al. was subsequently generalized to three dimensions by Kim et al. [18] in an LES, again for an axisymmetric jet. We adapt the model of Kim et al., and implement actuation in our twin-rectangular jet LES. From the LES, we collect a database on which to perform statistical analysis. For an axisymmetric jet, such analysis universally begins with an azimuthal Fourier transform, taking advantage of the spatial homogeneity of the turbulent statistics to vastly simplify the problem. Jets in the dihedral group D_2, including rectangular, elliptic, and twin jets, are inhomogeneous. In order to interpret the flow instabilities at play in the twin-rectangular jet rigorously, we apply D_2-symmetry decomposition—a technique we recently demonstrated on the unforced case [15]. Once D_2 symmetry has been enforced, we perform bispectral mode decomposition (BMD) [19] on the symmetry components. BMD extends SPOD to third-order statistics. A triad consists of frequencies $\{f_j, f_k, f_l\}$ that satisfy the zero-sum condition,

$$f_j \pm f_k \pm f_l = 0. \tag{1}$$

BMD extracts structures involved in triadic interactions by detecting quadratic phase-coupling among modes oscillating at frequencies that satisfy this condition. Successfully used to study the generation of harmonics and resonances in flows including round jets [20] and two-phase swirling flows [21], BMD is also the ideal tool with which to study the nonlinear dynamics of the forced twin-rectangular jet flow.

This paper is organized as follows. In Section II.A, we recapitulate the LES setup of the natural jet, in continuation from Brès et al. [13, 14] and Yeung et al. [15]. Section II.B describes the numerical modeling of LAFPAs in the forced jet. In Section III.A, we introduce the D_2-symmetry decomposition that will be applied to both the natural and forced jet data. We briefly review BMD in Section III.B. Analysis of the forced jet is presented in Section IV, followed by a summary of the conclusions in Section V.

II. Numerical setup

A. Large-eddy simulation

The twin-rectangular jet, with a design Mach number of $M_d = 1.5$, was set up by Esfahani et al. [22] at OSU's experimental facility. Using the unstructured, compressible LES solver 'Charles' developed by Cascade Technologies [23], we recently simulated this jet in its baseline configuration, i.e., without plasma actuation [13, 15]. The simulation is normalized by the ambient conditions, ρ_∞, T_∞, and $c_\infty = \sqrt{\gamma p_\infty/\rho_\infty}$. Lengths are normalized by the nozzle height, h. The jet is nominally ideally-expanded and cold, with nozzle exit conditions $M_j = U_j/c_j = 1.5$, $p_j/p_\infty = 1$, $T_j/T_\infty = 0.69$, and $Re_j = \rho_j U_j D_e/\mu_j = 1.07 \times 10^6$, where $D_e = 1.6h$. The nozzle pressure and temperature ratios are $p_t/p_\infty = 3.671$ and $T_t/T_\infty = 1$, respectively. The nozzle geometry, which is explicitly included in the computational domain, closely matches OSU's experimental setup. As shown in Fig. 1, each of the twin nozzles has a groove cut into the internal wall just upstream of the nozzle exit. Housed within the groove are eight pairs of electrodes per nozzle, allowing for a maximum of eight plasma actuators per nozzle. The computational grid, shown in Fig. 2, contains approximately 77 million cells. The parameters of the baseline simulation are summarized in Table 1; for full details, including the validation of the simulation against companion experiments at OSU, we refer the reader to Brès et al. [13].

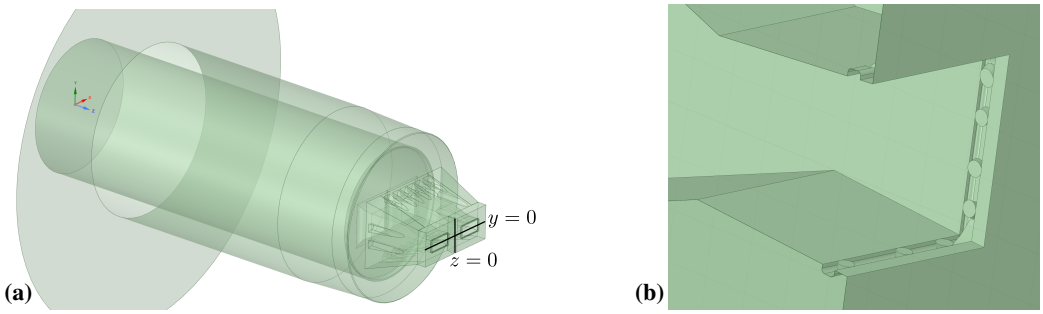

Fig. 1 Nozzle geometry [13]: (a) exterior view of the twin nozzles; (b) interior view of one nozzle, showing the electrodes recessed into a groove near the exit. The major ($y = 0$) and minor ($z = 0$) axes are also displayed.

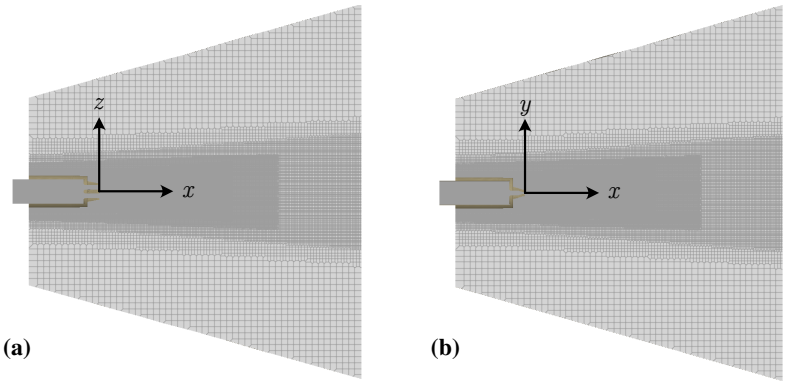

Fig. 2 Computational grid of the baseline LES: (a) horizontal cut through the center lines of both nozzles, i.e., the major-axis plane; (b) vertical cut through the center line of a single nozzle, parallel to the minor-axis plane.

B. Modeling of plasma actuation

To implement plasma actuators in the twin-rectangular jet, we adapt the model proposed by Kim et al. [18]. Extending our previous work in actuator modeling [13], we insert a volumetric energy source term,

$$S(x, y, z, t) = k(t)l(r)m(z)\frac{P}{\pi r_0^2 L}, \tag{2}$$

where P is an amplitude with dimensions of power, into the right-hand side of the energy equation. Note that for notational simplicity, the axis of the plasma arc is aligned with the z-axis; in actual implementation, the orientation of the arc—and therefore of the energy source—is aligned with the groove around the nozzle lip. The spatial support is in the form of a cylinder of radius r_0 and length L, and is expressed as the product of

$$l(r) = \frac{1}{2}\left[\tanh\left(-\sigma\left(\frac{r}{r_0} - \frac{1}{2}\right)\right) + 1\right] \tag{3}$$

and

$$m(z) = -\frac{1}{2}\left[\tanh\left(-\sigma\frac{z + L/2}{r_0}\right) + 1\right] + \frac{1}{2}\left[\tanh\left(-\sigma\frac{z - L/2}{r_0}\right) + 1\right], \tag{4}$$

where $r = \sqrt{x^2 + y^2}$, and σ controls the sharpness of the cylindrical boundary. The energy source is modulated in time by the signal

$$k(t) = \frac{1}{2}\left[\tanh\left(\frac{(t - n\tau) - t_{\text{on}}}{t_r}\right) - \tanh\left(\frac{(t - n\tau) - t_{\text{off}}}{t_r}\right)\right], \tag{5}$$

where t_{on} and t_{off} are the time instants within each forcing period at which the signal is switched on and off, respectively, t_r is the rise time, τ is the forcing period, and $n = \lfloor t/\tau \rfloor$. Thus $k(t)$ is a smoothed square wave.

We assume r_0 to be half the height of the groove, and L to be the centroid-to-centroid distance between a pair of electrodes. σ is taken from Kim et al. [18]. The choice of forcing amplitude P, and temporal parameters t_{on}, t_{off}, and t_r,

Table 1 LES parameters.

Case	M_j	M_a	Re_j	p_t/p_∞	p_j/p_∞	T_t/T_∞	T_j/T_∞	N_{cv}	$\mathrm{d}tc_\infty/h$
Baseline	1.5	1.25	1.07×10^6	3.671	1	1	0.69	76.6×10^6	0.002
Forced	1.5	1.25	1.07×10^6	3.671	1	1	0.69	77.0×10^6	0.001

Table 2 Nondimensionalized plasma actuation parameters. Ambient temperature and pressure are assumed to be 293 K and 1 atm, respectively. The spatial support of the volumetric energy source that models a plasma arc is a cylinder of length L and radius r_0. For notational simplicity, the origin is taken to be the centroid of the plasma arc, and the z-axis refers to the direction aligned with the groove around the nozzle lip.

Case	$P/\rho_\infty c_\infty^3 h^2$	r_0/h	L/h	σ	$t_{\mathrm{on}}c_\infty/h$	$t_{\mathrm{off}}c_\infty/h$	$t_r c_\infty/h$	St_0
Forced	17.44	0.02	0.29	5	0	0.0015	2×10^{-5}	0.29

is based on voltage and current measurements by Samimy et al. (private communication) of a typical actuation cycle. The actuators are assumed to be 100% power-efficient. When nondimensionalized, the duty cycle, $t_{\mathrm{off}} - t_{\mathrm{on}}$, is measured to be on the order of one LES time step, though this is likely an overestimate due to finite sampling frequency. The rise time, t_r, is chosen to be much smaller than the LES time step so that the actuators respond effectively instantaneously. In general, these modeling parameters can be set independently for each actuator; in this paper, however, all actuators behave identically, except for potential phase differences between their actuation cycles. The modeling parameters are summarized in Table 2. In our previous plasma modeling effort, we also observed a strong dependence of control authority on the local grid resolution in and around the groove [13]. We therefore introduce additional grid refinement to the vicinity of the groove, locally reducing the average cell width by a factor of two, as shown in Fig. 3. Due to explicit time-stepping, this necessitated a smaller time step, though the overall grid size remains approximately 77 million (see Table 1). Since it is challenging to obtain direct measurements of the local flow environment around a plasma arc, rather than attempt to replicate a specific experiment, we seek to demonstrate the control authority of plasma actuation by exciting specific modes of instability in the twin-rectangular jet. We will return to this point in Section III.A.

III. Statistical analysis

A. D_2-symmetry decomposition

In turbulent flows that enjoy (statistical) homogeneity in one or more spatial directions, prior to the application of modal decomposition we Fourier-transform the data along the homogeneous directions. Doing so reduces computational effort, accelerates the convergence of the statistics, and most importantly, enhances the interpretability of the results. For axisymmetric jets, this procedure amounts to an azimuthal Fourier transform, which enables us to analyze a set of two-dimensional azimuthal Fourier modes. Twin jets, on the other hand, are triply inhomogeneous flows. Instead they possess D_2 symmetry, i.e., their geometries are invariant under reflection about the major and minor axes. In such flows, D_2 symmetry gives rise to four symmetry components [24–26]: SS, SA, AS, and AA, where the first and second letters denote symmetry (S) or antisymmetry (A) about the major and minor axes, respectively [27].

By analogy to the azimuthal Fourier transform of axisymmetric jets, a rigorous statistical analysis of twin jets must account for their geometrical symmetries. In our previous work, we proposed a D_2-symmetry decomposition of twin jet flows into the four symmetry components. For a detailed discussion of the D_2-symmetric workflow, we refer the reader to Yeung et al. [15]; here we briefly outline the main steps. We begin by estimating the long-time mean, $\overline{\mathbf{q}}$, which is SS-symmetric. To do so, we enforce SS symmetry on the sample mean, and obtain an improved estimate, $\overline{\mathbf{q}}_{\mathrm{SS}}$. Using $\overline{\mathbf{q}}_{\mathrm{SS}}$, we apply the Reynolds decomposition to the instantaneous data, and find the turbulent fluctuations,

$$\mathbf{q}'(x,y,z,t) = \mathbf{q}(x,y,z,t) - \overline{\mathbf{q}}_{\mathrm{SS}}(x,y,z)\,. \tag{6}$$

Next, we enforce D_2 symmetry on $\mathbf{q}'$, and decompose it into four symmetry components:

$$\mathbf{q}'(x,y,z,t) = \mathbf{q}'_{\mathrm{SS}}(x,y,z,t) + \mathbf{q}'_{\mathrm{SA}}(x,y,z,t) + \mathbf{q}'_{\mathrm{AS}}(x,y,z,t) + \mathbf{q}'_{\mathrm{AA}}(x,y,z,t)\,. \tag{7}$$

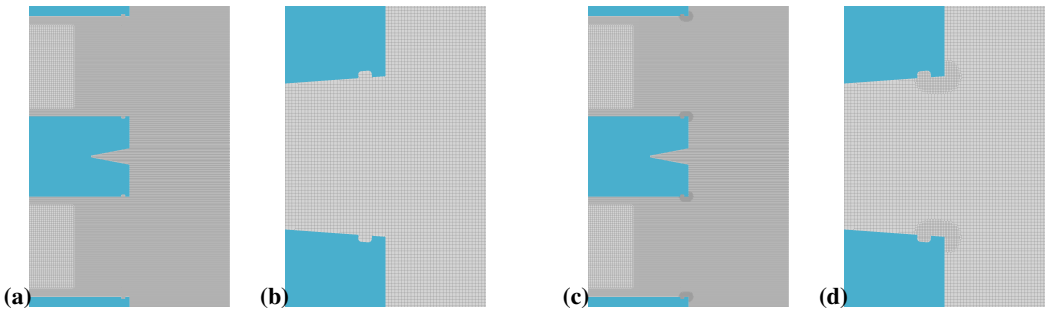

Fig. 3 Local grid refinement around the groove: (a,b) baseline case; (c,d) forced case. (a,c) show a horizontal cut through the center lines of both nozzles, i.e., the major-axis plane; (b,d) zoom in on a vertical cut through the center line of a single nozzle, parallel to the minor-axis plane.

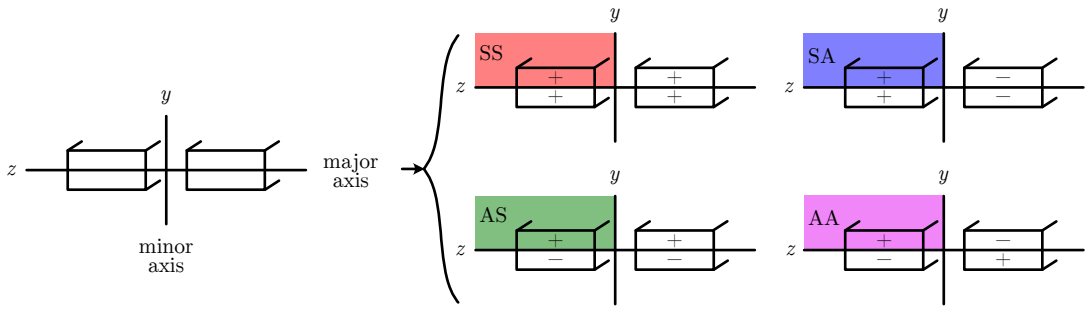

Fig. 4 D_2-symmetry decomposition [15]. For each symmetry component, three of the four quadrants contain redundant information. Without loss of generality, we perform modal decomposition only on the first quadrant.

For each component or set of multiple components, solving a modal decomposition problem leads to three-dimensional modes, thus concluding the workflow. Note that, as implied by Eq. (7), D_2 decomposition leads to no loss of generality: $\mathbf{q}'$ can be exactly reconstructed by summing the four components. Figure 4 summarizes this decomposition.

In our recent analysis of the natural twin-rectangular jet, D_2-symmetric SPOD revealed that the AA and AS components emit a fundamental screech tone at $St = 0.29$, while the SS and SA components do not [15]. In this paper, we demonstrate the excitation of SS-symmetric instabilities using plasma actuation, and explore the potential for such excitation to disrupt the preferred symmetry components of the natural jet. The experiments of Esfahani et al. [28] employed six actuators per nozzle—three on the top lip, three on the bottom lip—and forced the jet at its natural screech frequency. We adopt a similar strategy; specifically, to achieve SS excitation, all 12 actuators will fire in-phase, at frequency $St = 0.29$ (see Table 2). We denote the forcing frequency by f_0 or, equivalently, St_0.

B. Bispectral mode decomposition

The unstructured LES snapshots are interpolated onto a Cartesian grid for postprocessing. The database and spectral estimation parameters are provided in Table 3. To compute BMD [19] for the frequency triad (f_k, f_l, f_{k+l}), we assemble

Table 3 Interpolation and spectral estimation parameters.

	Database								Parameters		
Case	N_x	N_y	N_z	$[x_{\min}, x_{\max}]$	$[y_{\min}, y_{\max}]$	$[z_{\min}, z_{\max}]$	N_t	$\Delta t c_\infty / h$	N_{FFT}	N_{ovlp}	N_{blk}
Natural	625	270	344	$[0, 85h]$	$[-16h, 16h]$	$[-16h, 16h]$	20000	0.2	1024	512	38
Forced	625	270	344	$[0, 85h]$	$[-16h, 16h]$	$[-16h, 16h]$	10000	0.2	1024	512	18

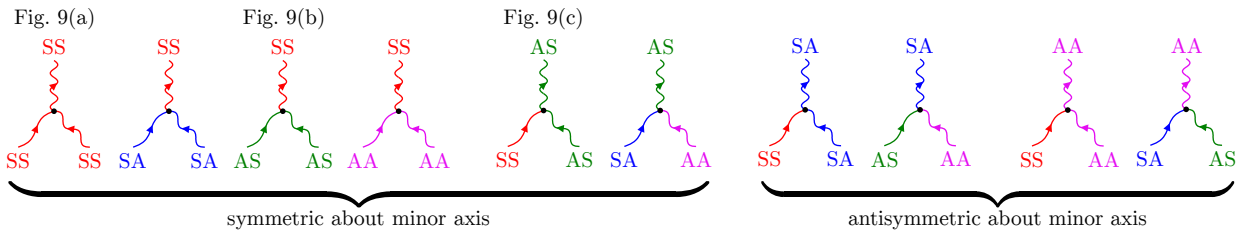

Fig. 5 Triadic interactions between modes with the same symmetry (auto-BMD) or different symmetries (cross-BMD).

the data matrices

$$\hat{\mathbf{Q}}_{k\circ l} = \left[\hat{\mathbf{q}}_{k\circ l}^{(1)} \quad \hat{\mathbf{q}}_{k\circ l}^{(2)} \quad \cdots \quad \hat{\mathbf{q}}_{k\circ l}^{(N_{\text{blk}})}\right] \tag{8}$$

and

$$\hat{\mathbf{Q}}_{k+l} = \left[\hat{\mathbf{q}}_{k+l}^{(1)} \quad \hat{\mathbf{q}}_{k+l}^{(2)} \quad \cdots \quad \hat{\mathbf{q}}_{k+l}^{(N_{\text{blk}})}\right], \tag{9}$$

where $\hat{\mathbf{q}}_{k\circ l} = \hat{\mathbf{q}}(f_k) \circ \hat{\mathbf{q}}(f_l)$, $\hat{\mathbf{q}}_{k+l} = \hat{\mathbf{q}}(f_{k+l})$, and $\circ$ denotes the Hadamard product. In the case of the auto-BMD, $\hat{\mathbf{q}}(f_k)$, $\hat{\mathbf{q}}(f_l)$, and $\hat{\mathbf{q}}(f_{k+l})$ possess the same symmetry. Conversely, in cross-BMD they come from multiple symmetry components. Next we form the bispectral density matrix,

$$\mathbf{B} = \frac{1}{N_{\text{blk}}}\hat{\mathbf{Q}}_{k\circ l}^H \mathbf{W}\hat{\mathbf{Q}}_{k+l}, \tag{10}$$

where $\mathbf{W}$ is the numerical quadrature weight matrix. Solving the numerical radius problem for $\mathbf{B}$ results in the expansion coefficients

$$\mathbf{a}_1 = \arg\max_{\mathbf{a}} \left|\frac{\mathbf{a}^H\mathbf{B}\mathbf{a}}{\mathbf{a}^H\mathbf{a}}\right| \tag{11}$$

and complex mode bispectrum

$$\lambda_1 = \frac{\mathbf{a}_1^H\mathbf{B}\mathbf{a}_1}{\mathbf{a}_1^H\mathbf{a}_1}. \tag{12}$$

Finally, the BMD modes are recovered as $\boldsymbol{\phi}_{k+l} = \hat{\mathbf{Q}}_{k+l}\mathbf{a}_1$. Interactions between symmetry components can give rise to new symmetries; all non-redundant combinations of symmetries in a triad are illustrated in Fig. 5.

IV. Results

Figure 6 visualizes the instantaneous temperature of the SS-symmetrically forced jet, over one representative forcing cycle. Although the jet is nominally ideally-expanded based on the nozzle-exit pressure, the potential cores contain shock diamonds as a result of the biconical nozzles as well as the grooves immediately upstream of the nozzle lips. 6(a,b) capture the instant at which all actuators fire simultaneously. A localized burst of high temperature (white) is visible at each nozzle lip in 6(a); this near-nozzle effect is not readily apparent in 6(b) because the major-axis plane does not intersect any actuators. However, both views show the roll-up of regularly-spaced vortices further from the nozzle as the initial effects of the actuation become amplified via the KH instability [29]. The large vortices are symmetric about both the major and minor axes, confirming the SS-symmetric forcing.

The difference between the long-time mean streamwise velocities of the forced and natural jets, $U_{\text{forced}} - U_{\text{natural}}$, is shown in Fig. 7. The $z = 1.8$ and $y = 0$ planes in 7(a,b) confirm the shear-layer thickening observed in the instantaneous temperature field in Fig. 6, in the form of acceleration of the ambient flow due to increased entrainment. This thickening is asymmetric with respect to each lip line. In 7(a), for instance, the enhanced growth of the initial shear layer is restricted to $|y| > 0.5$, i.e., the regions above the upper lip line and below the lower lip line. Similarly, in 7(b) the initial shear layers grow much more rapidly in the regions that consist of $|z| < 0.8$ (between the inner lip lines) and $|z| > 2.8$ (outside the outer lip lines). Although all the actuators are located on the nozzle lips corresponding to $y = \pm 0.5$ (7(a)), the shear layers emanating from the $z \in \{\pm 0.8, \pm 2.8\}$ nozzle lips (7(b)) display more pronounced forcing-induced growth. Compared to the natural jet, faster shear-layer growth in the $y = 0$ plane leads to merging of the twin jet plumes at a more upstream location, potentially encouraging stronger inter-jet coupling.

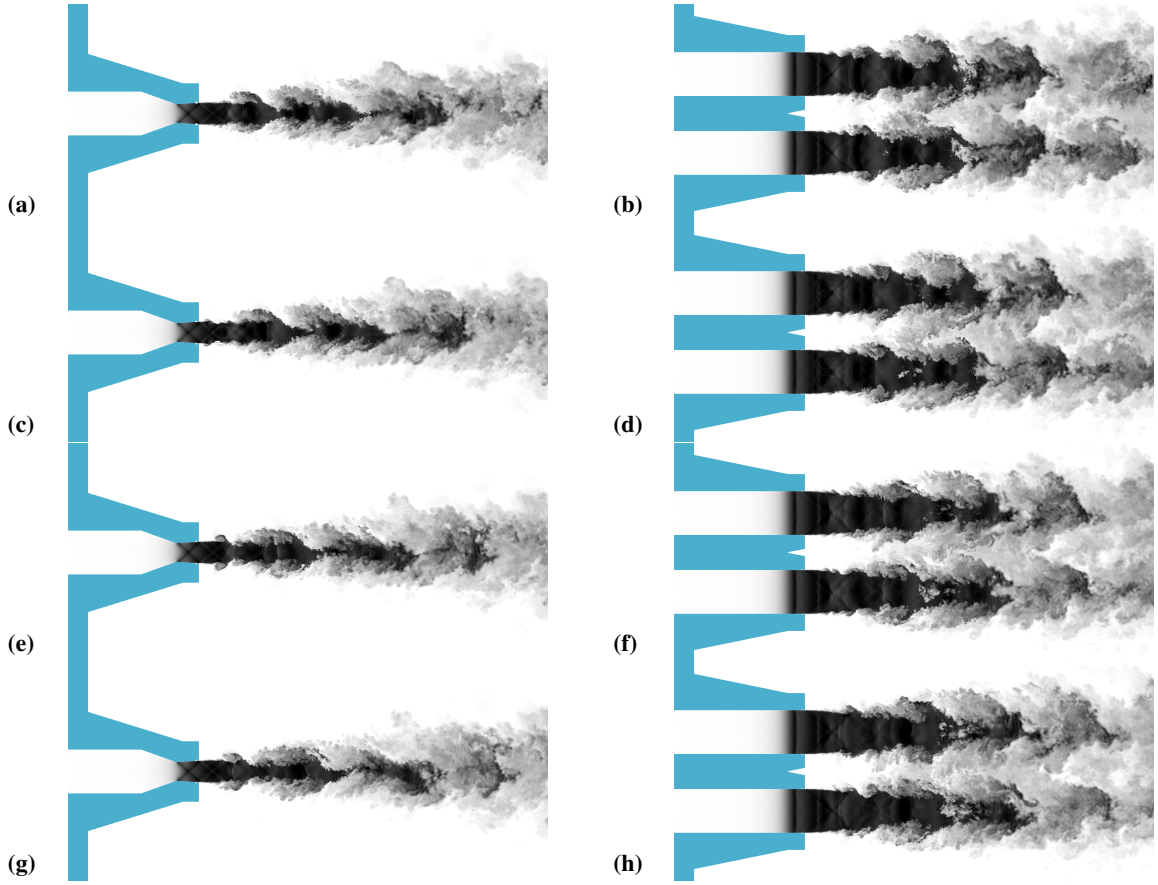

Fig. 6 Instantaneous temperature (■ $0.65 \le T/T_\infty \le 0.99$) over one forcing period: (a,c,e,g) $z/h = 1.8$ plane through the center line of a single nozzle, parallel to the minor-axis plane; (b,d,f,h) major-axis plane. Actuators fire in (a,b). Each successive row advances by a phase of $\pi/2$.

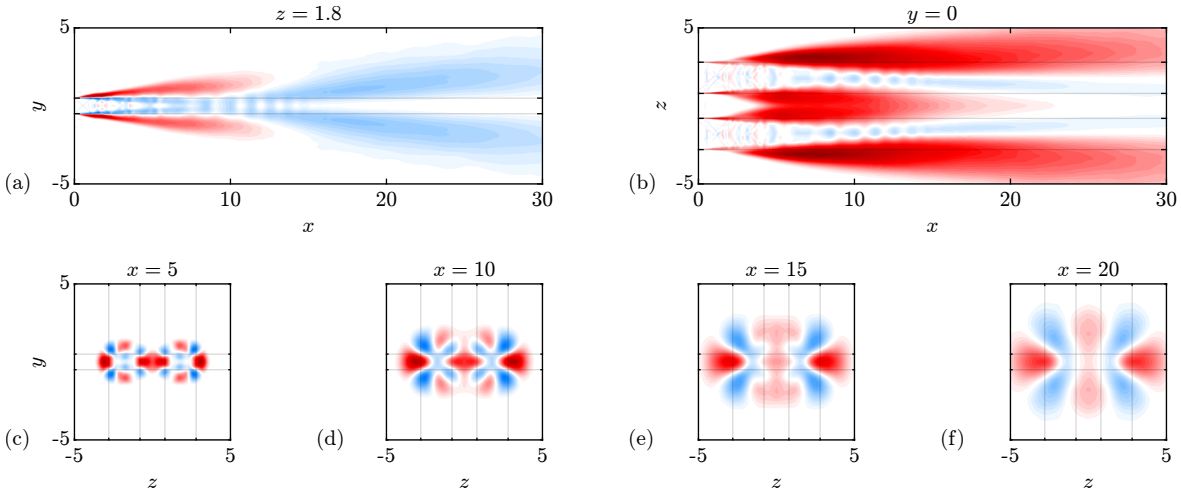

Fig. 7 The effect of forcing on the long-time mean streamwise velocity (■ $-0.25 \le (U_{\text{forced}} - U_{\text{natural}})/U_j \le 0.25$): (a) $z = 1.8$ plane, parallel to the minor axis; (b) major-axis plane; (c–f) transverse planes at $x \in \{5, 10, 15, 20\}$. The lip lines, located at $y = \pm 0.5$ and $z \in \{\pm 0.8, \pm 2.8\}$, are marked by gray lines.

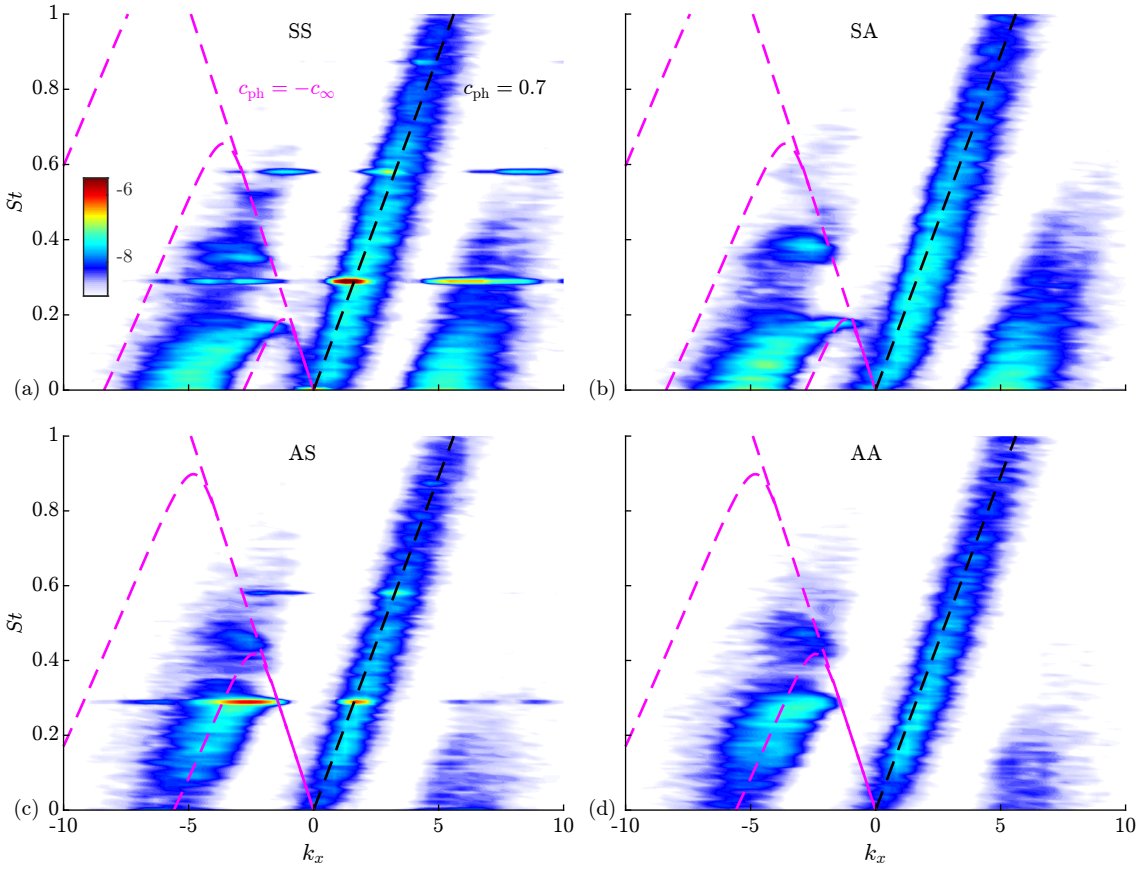

Fig. 8 Frequency-wavenumber diagrams, $\log_{10}|\hat{p}_{\omega k_x}|^2$, of the forced jet computed from pressure fluctuations along the line $5 < x < 20$, $y = 0.25$, $z = 1.8$: (a) SS; (b) SA; (c) AS; (d) AA symmetry components. All symmetries share the same colorbar. Lines of constant phase speed (– – –, $c_{\mathrm{ph}} = 0.7$) and (– – –, $c_{\mathrm{ph}} = -c_\infty$) are overlaid on the contours. The vortex sheet model of Tam and Norum [30] is also shown (– – –): (a,b) symmetric mode; (c,d) antisymmetric mode.

Within each potential core, the forced jet velocity experiences greater deceleration as the jet transits the series of shock cells. This is indirect evidence for increased shock strength in the forced jet, possibly as a consequence of constructive interactions between the stationary shocks and the moving shock fronts generated by the actuators. Beyond the initial shear layer, the velocity difference in the $z = 1.8$ plane can be divided into two distinct regions: $x \lesssim 12$, in which the forced jet is accelerated, and $x \gtrsim 12$, in which the forced jet is decelerated, relative to the natural jet. The switch at $x \approx 12$ in the $z = 1.8$ plane approximately coincides with the point at which the inner shear layers of the twin jets become fully merged in the $y = 0$ plane. The sequence of transverse views in 7(c–f), at distances $x \in \{5, 10, 15, 20\}$, provides further insight into the streamwise evolution of the velocity difference. At $x \in \{5, 10\}$, the center of each nozzle lip is aligned with regions of increased velocity due to enhanced entrainment. The corners are aligned with regions of decreased velocity due to the reinforced shocks, which form an 'X' pattern in front of each nozzle. At $x \in \{15, 20\}$, the twin jets are merged along the minor axis, $z = 0$. In the inter-nozzle space, $|z| < 0.8$, and in the regions $|z| > 2.8$, the forced jet is primarily accelerated. In the regions $0.8 < z < 2.8$ and $-2.8 < z < -0.8$, the forced jet is primarily decelerated. This intricate (y, z)-dependence of the long-time mean, which cannot be captured by an individual azimuthal Fourier mode, underscores the necessity of performing D_2-symmetry decomposition.

To examine the effects of forcing on the temporal and spatial scales in each of the four symmetry components, in Fig. 8 we plot contours of the power spectral density (PSD), $|\hat{p}_{\omega k_x}|^2$, where ω is the angular frequency, and k_x the streamwise wavenumber. To compute $\hat{p}_{\omega k_x}$, we take the double Fourier transform of pressure fluctuations in time and space. The temporal transform employs Welch-averaging to reduce variance [31]. The spatial transform is taken along the line $(y, z) = (0.25, 1.8)$, constrained to $5 < x < 20$, which gives the clearest spectral shapes. The spatiotemporal

PSD can be interpreted as an empirical dispersion relation. Since only $St \geq 0$ is shown, the $k_x > 0$ and $k_x < 0$ half-planes represent waves with positive and negative phase velocities, ω/k_x, respectively. Positive and negative slopes, on the other hand, represent waves with positive and negative group velocities, $\partial\omega/\partial k_x$, respectively. Common to all four symmetries is the band of constant phase speed, $c_{\text{ph}} = 0.7$, corresponding to the typical convection velocity of KH modes. For SS and AS symmetries (8(a,c)), along the KH band the PSD peaks at $f = 0$, the forcing frequency f_0, and its superharmonics. In the $k_x < 0$ half-plane, the bands are largely restricted to the domain $\omega/k_x > -c_\infty$, i.e., waves with negative phase velocities propagate at less than the ambient speed of sound. In the SS and SA components (8(a,b)), for $St < 0.2$ the upstream-propagating band is curved. The group velocity, which is positive, decreases with frequency and approaches zero as $St \to 0.2$. In the SS component, there is also a peak at $St \approx 0.35$. The peaks at f_0 and its harmonics, on the other hand, are likely the result of aliasing from the KH band. In the SA symmetry, there is a similar peak, but at a higher frequency, $St \approx 0.4$. The band to the right of the KH modes in the $k_x > 0$ half-plane is the extension of the upstream-propagating band into negative frequencies; their appearance in the $k_x > 0$ half-plane is a consequence of the conjugate symmetry between the quadrants $(f > 0, k_x > 0)$ and $(f < 0, k_x < 0)$, and between $(f > 0, k_x < 0)$ and $(f < 0, k_x > 0)$. In the AS and AA components (8(c,d)), the upstream-propagating band possesses no pronounced curvature, and terminates at a higher frequency than in SS and SA, approximately at f_0. As with SS and SA, in AS and AA there is also a higher-frequency peak, at $St \approx 0.5$. Unique to AS, there is a prominent peak at f_0 in the $k_x < 0$ half-plane. Since only SS is forced, this peak in AS corresponds to the natural screech tone.

Next we compare the empirical dispersion relation of the upstream-propagating waves to the analytical predictions of the two-dimensional vortex sheet model of Tam and Norum [30] for rectangular jets. The dispersion relations of the model are given by

$$\frac{\left[\frac{(\omega-U_j k_x)^2}{c_j^2} - k_x^2\right]^{1/2} \rho_\infty \omega^2}{\left(k_x^2 - \frac{\omega^2}{c_\infty^2}\right)^{1/2} \rho_j (\omega - U_j k_x)^2} - \cot\left\{\left[\frac{(\omega - U_j k_x)^2}{c_j^2} - k_x^2\right]^{1/2} \frac{h}{2}\right\} = 0 \tag{13}$$

for symmetric modes, and

$$\frac{\left[\frac{(\omega-U_j k_x)^2}{c_j^2} - k_x^2\right]^{1/2} \rho_\infty \omega^2}{\left(k_x^2 - \frac{\omega^2}{c_\infty^2}\right)^{1/2} \rho_j (\omega - U_j k_x)^2} + \tan\left\{\left[\frac{(\omega - U_j k_x)^2}{c_j^2} - k_x^2\right]^{1/2} \frac{h}{2}\right\} = 0 \tag{14}$$

for antisymmetric modes. As a two-dimensional model cannot distinguish between symmetry and antisymmetry about the minor axis, we compare symmetric modes with both SS and SA components, and antisymmetric modes with both AS and AA components. The solutions to Eqs. (13) and (14) are plotted in Fig. 8 accordingly. In 8(a,b), the symmetric Tam and Norum (TN) modes accurately predict the maximum frequency attained by the upstream-propagating waves, but underpredicts their wavenumbers. For $St < 0.2$, the PSD also shows significant dispersion and a group velocity that is frequency-dependent, neither of which is captured by the model. In 8(c,d), the antisymmetric TN modes approximately predict the wavenumbers in the PSD at each frequency, but only up to f_0. Unlike the symmetric mode, for $St < 0.4$ the constant group velocity of the antisymmetric mode is consistent with the PSD. Both symmetric and antisymmetric TN modes allow for waves with negative group velocities; however, we do not observe such waves in the PSDs. Taken together, these discrepancies hint at the limited applicability of two-dimensional models to rectangular jets of moderate aspect ratio.

The SS-self interactions are educed using auto-BMD and reported in Fig. 9(a). The AS-self interactions and SS-AS interactions are educed using cross-BMD and reported in Figs. 9(b) and 9(c), respectively. The remaining bispectra, involving the SA and AA components, have lower magnitudes and are thus less dynamically relevant. For each bispectrum, only the non-redundant region is displayed. The bispectra in 9(a,b) are triplets in which the Fourier realizations $\hat{\mathbf{q}}_k$ and $\hat{\mathbf{q}}_l$ possess the same symmetry. The white region, $(f_1 > 0, f_2 > f_1)$, can be recovered through reflection of the principal region, $(f_1 > 0, 0 < f_2 < f_1)$, about the red line, $f_2 = f_1$. The gray region, $(f_1 > 0, f_2 < -f_1)$, can be recovered through reflection of the region $(f_1 > 0, -f_1 < f_2 < 0)$ about the blue line, $f_2 = -f_1$, followed by complex conjugation. In contrast, for the bispectrum in 9(c), the Fourier realizations $\hat{\mathbf{q}}_k$ and $\hat{\mathbf{q}}_l$ have different symmetries. The gray region, $(f_1, f_2 < -f_1)$, can be recovered from the region $(f_1, f_2 > -f_1)$ via a reflection about $f_1 = 0$, then another reflection about $f_2 = 0$, followed by complex conjugation.

The most dominant triads in Fig. 9 form the usual grid pattern. When sign f_1 = sign f_2, sum interactions generate superharmonics of the forcing or screech frequency, f_0. Conversely, when sign $f_1 = -$ sign f_2, difference interactions

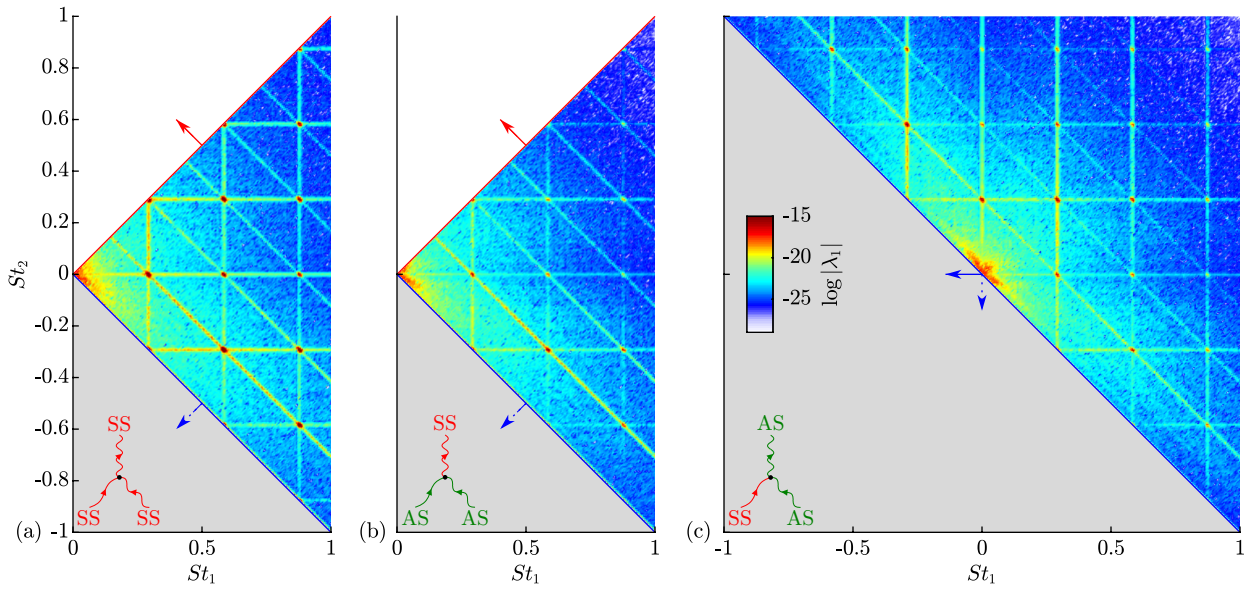

Fig. 9 Modulus of the BMD complex mode bispectra of the forced jet, computed using the pressure 2-norm: (a) auto-BMD of the SS component; (b,c) cross-BMD involving the SS and AS components. All bispectra share the same colorbar. Only the non-redundant region of each bispectrum is shown. Solid arrows (—►) denote reflection of the non-redundant region; dotted arrows (· · ·►) denote reflection followed by conjugation.

generate modes at lower frequencies. Triads that lie on the line $f_3 = f_1 + f_2 = 0$ represent mean-flow deformation. In Figs. 10–13, we study these quadratic interactions in greater detail.

Figure 10 shows a representative selection of dominant triadic interactions of the [[SS, SS, SS]] symmetry triplet. Starting with sum interactions, in 10(a) the linear mode at the fundamental forcing frequency, f_0, self-interacts to form the first superharmonic at frequency $2f_0$. In 10(b), the first superharmonic further self-interacts to form the third superharmonic at $4f_0$. In 10(c), the forcing interacts with the first superharmonic to generate the second superharmonic at $3f_0$. In 10(d), the forcing undergoes difference-self-interaction with its complex conjugate to generate a mean flow distortion. The corresponding bispectral modes are reported in Fig. 11.

The linearly forced mode, $(f_0, 0)$, in Fig. 11(a,c,d) reveal the KH instability waves created by the actuators, which couple the twin jets symmetrically about the minor axis. From this fundamental mode, the forward cascade leads to the formation of higher-frequency and higher-wavenumber structures (11(a,b,c)). The superharmonic modes contain KH wavepackets in the initial shear layers. The spatial support of these wavepackets is restricted further upstream with increasing frequency. The mean flow distortion in 11(d) appears to be active primarily in the shear layers, outside the potential cores.

Next we illustrate the dominant triadic interactions that involve both SS- and AS-symmetric modes in Fig. 12. The AS-symmetric linear mode, $(f_0, 0)$, contribute to the triads in 12(a,b,c,e,f). Unlike the SS symmetry component, the AS symmetry is unforced. We therefore identify the AS $(f_0, 0)$ mode with the naturally-occurring, fundamental screech tone at frequency f_0. In 12(a), the AS fundamental screech self-interacts to form the first SS superharmonic. The formation of the first AS superharmonic, on the other hand, relies on the cross-symmetry interaction between the SS forcing and AS screech modes, as shown in 12(b). In 12(c) the fundamental screech interacts with the AS first superharmonic, generating the SS second superharmonic. Conversely, in 12(d) the fundamental forcing interacts with the AS first superharmonic to generate the AS second superharmonic. 12(e) shows the difference-self-interaction of the fundamental screech, resulting in mean flow distortion of the SS symmetry. 12(f) shows the difference interaction between the screech and the conjugate of the forcing, causing deformation of the AS mean flow.

Figure 13 shows the corresponding mode shapes. Analogous to the auto-BMD of the SS component, the forward cascade of cross-bispectral triads forms higher-frequency modes that contain higher-wavenumber structures. A noteworthy difference is that the AS $(-f_0, f_0, 0)$ mean flow distortion has its maximum amplitude not in the shear layer, but within the potential core, where the mode recovers the shape of the shock cells.

To understand why the [[SS, SS, SS]], [[AS, AS, SS]], and [[SS, AS, AS]] symmetry triplets bear the clearest

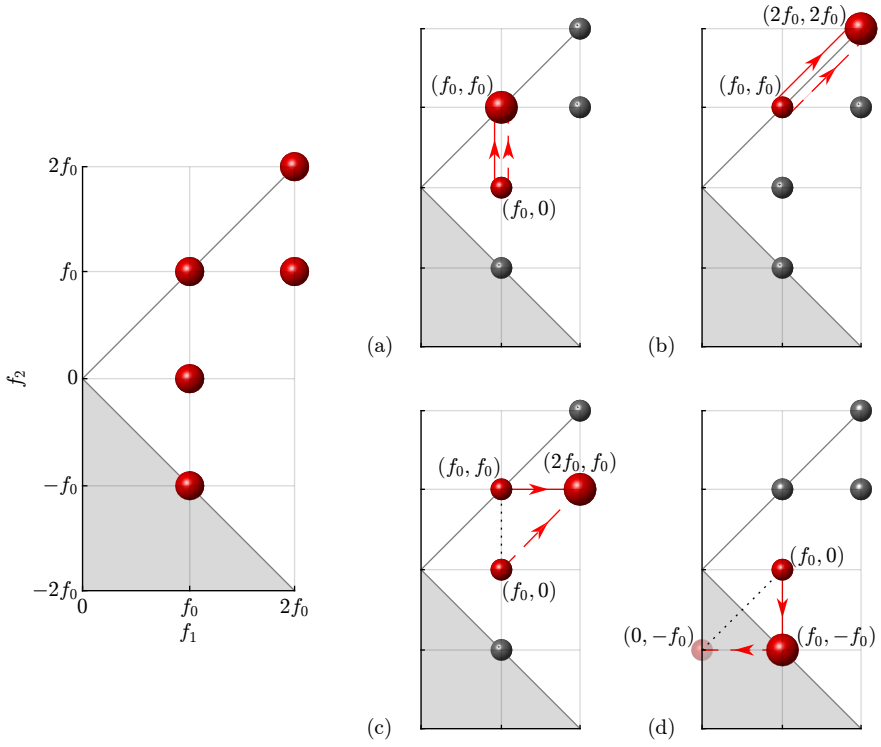

Fig. 10 Five representative triads from the [[SS, SS, SS]] BMD auto-bispectrum in Fig. 9(a), reproduced on the left. To the right, red spheres highlight the generation of the following triads: (a) $(f_0, f_0, 2f_0)$; (b) $(2f_0, 2f_0, 4f_0)$; (c) $(2f_0, f_0, 3f_0)$; (d) $(f_0, -f_0, 0)$. In each subplot, the large sphere indicates the mode corresponding to f_{k+l}. Solid (——) and dashed (– – –) lines distinguish between f_k and f_l, respectively. Dotted lines (· · · · · ·) connect f_k to f_l. Arrows point towards or away from f_{k+l} in sum or difference interactions, respectively. The translucent sphere denotes the complex conjugate of the mode in the non-redundant region.

signatures of triadic interactions, we consider the summed mode spectra of the remaining triplets. A summed mode spectrum provides an overview of which frequencies f_{k+l} are involved in quadratic phase coupling, without distinguishing between the contributing frequencies, f_k and f_l. It is the average of the mode bispectrum along each constant-f_3 diagonal [19], i.e.,

$$\Lambda_1(f_3) = \frac{1}{N(f_3)} \sum_{f_3=f_1+f_2} |\lambda_1(f_1, f_2)|\,, \tag{15}$$

where $N(f_3)$ is the number of triads along the diagonal. The results are shown in Fig. 14. Consistent with the bispectra in Fig. 9, the aforementioned triplets involving SS and/or AS symmetries show peaks at $f_3 = nf_0$, where $n = 0, 1, 2, \ldots$ The same peaks, albeit less dominant, also appear in the summed mode spectra of the [[SA, SA, SS]], [[AA, AA, SS]], and [[SA, AA, AS]] triplets. The absence of dominant triads in their respective bispectra (not shown) suggests the SA and/or AA symmetries are merely phase-coupled rather than interacting. The remaining four triplets do not show peaks in their summed mode spectra: [[SS, SA, SA]], [[AS, AA, SA]], [[SS, AA, AA]], and [[SA, AS, AA]]. In each of these triplets, modes f_k and f_l have opposing symmetries about the minor axis. Specifically, whereas SS and AS are symmetric about the minor axis, SA and AA are antisymmetric about the minor axis. Under SS-symmetric forcing, only when two modes have the same symmetry about the minor axis are they capable of phase-coupling and, potentially, nonlinearly interacting.

V. Summary and conclusions

Motivated by the desire to achieve noise reduction in military-style supersonic jet flows, we carried out LES of a plasma-actuated supersonic twin-rectangular jet. 12 actuators, modeled as energy source terms, around the exits of both nozzles pulsed in-phase with each other, imparting thermal and pressure perturbations to the jet shear layer. Due to

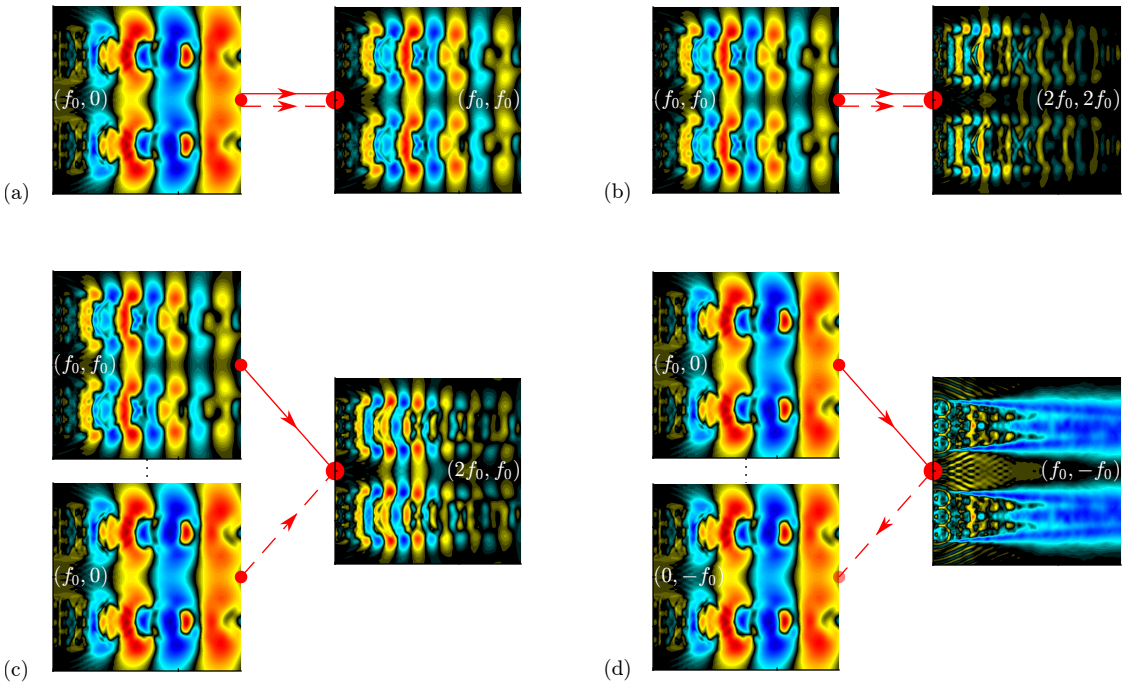

Fig. 11 Auto-bispectral modes of the [[SS, SS, SS]] triplet, corresponding to the triads in Fig. 10. The $y = 0.25$ plane is displayed. Only the real part of each mode is shown; consequently, in (d) the $(f_0, 0)$-mode appears identical to its complex conjugate, $(0, -f_0)$.

the in-phase forcing, these excitations were symmetric about the major and minor axes (i.e., SS-symmetric forcing) of the twin jet. A comparison between the long-time mean of the forced and natural jets confirm significant azimuthal inhomogeneity in the turbulent statistics, lending support to our use of D_2-symmetry decomposition. Frequency-wavenumber decomposition of the forced jet reveals the presence of downstream-propagating waves associated with the KH instability, as well as upstream-propagating waves. These waves, which have negative phase and positive group velocities, correspond only weakly to the two-dimensional vortex sheet model of Tam and Norum [30]. Discrepancies between the empirical and analytical dispersion relations call for the use of analytical frameworks that respect the D_2 symmetry of the twin jet in future modeling efforts. We further examined the impact of the SS-symmetric forcing on the dynamics of the twin jet with BMD. The BMD mode bispectra of the [[SS, SS, SS]], [[AS, AS, SS]], and [[SS, AS, AS]] symmetry triplets display dominant triadic interactions. The self-interactions of the SS forcing and of the AS natural screech tone generate superharmonics and mean flow distortion that are SS-symmetric. In contrast, cross-symmetry interactions between the SS forcing and AS screech form superharmonics and mean flow distortion that are AS-symmetric. The lack of SS-AS interactions could explain the absence of clear superharmonics in the AS component of the natural jet. The summed mode spectra of all non-redundant symmetry triplets indicate that when the jet is subjected to SS-symmetric forcing, quadratic phase-coupling between two modes is prevented from occurring if the modes possess inconsistent symmetries about the minor axis, i.e., one is symmetric about the minor axis while the other is antisymmetric. In other words, having the same minor-axis symmetry appears to be a necessary condition for two modes to undergo triadic interactions. We plan to investigate the generality of this observation by forcing the SA, AS, and AA components, as well as combinations thereof. In their experiments Samimy et al. [8] demonstrated the control authority of plasma actuators on twin-rectangular jet coupling (i.e., the recovery of symmetry or antisymmetry between the twin jets) and, in turn, the ability to manipulate near- and far-field noise. Understanding the extent to which symmetry incompatibility may forestall nonlinear interactions thus has practical implications for the design of effective control strategies for twin-jet noise reduction.

Acknowledgments

We gratefully acknowledge support from Office of Naval Research award N00014-20-1-2311, under the supervision of Dr. Steve Martens. LES calculations were carried out on the "Onyx" Cray XC40/50 system in ERDC DSRC, using allocations provided by DoD HPCMP.

References

[1] Heeb, N., Munday, D., Gutmark, E., Liu, J., and Kailasanath, K., "Supersonic Jet Noise Reduction by Chevrons Enhanced with Fluidic Injection," *AIAA paper 2010–4847*, June 2010. https://doi.org/10.2514/6.2010-4847.

[2] Henderson, B., and Bridges, J., "An MDOE Investigation of Chevrons for Supersonic Jet Noise Reduction," *AIAA paper 2010–3926*, June 2010. https://doi.org/10.2514/6.2010-3926.

[3] Bridges, J., Wernet, M. P., and Frate, F. C., "PIV measurements of chevrons on F400-series tactical aircraft nozzle model," *AIAA paper 2011–1157*, January 2011. https://doi.org/10.2514/6.2011-1157.

[4] Greska, B., Krothapalli, A., Seiner, J. M., Jansen, B., and Ukeiley, L., "The Effects of Microjet Injection on an F404 Jet Engine," *AIAA paper 2005–3047*, May 2005. https://doi.org/10.2514/6.2005-3047.

[5] Cattafesta III, L. N., and Sheplak, M., "Actuators for Active Flow Control," *Annual Review of Fluid Mechanics*, Vol. 43, January 2011, pp. 247–272. https://doi.org/10.1146/annurev-fluid-122109-160634.

[6] Samimy, M., Adamovich, I., Webb, B., Kastner, J., Hileman, J., Keshav, S., and Palm, P., "Development and characterization of plasma actuators for high-speed jet control," *Experiments in Fluids*, Vol. 37, 2004, pp. 577–588. https://doi.org/10.1007/s00348-004-0854-7.

[7] Prasad, A. L. N., and Nair, U. S., "Active Control of Noise in Supersonic Rectangular Jets," *APS Division of Fluid Dynamics Meeting Abstracts*, APS, November 2022.

[8] Samimy, M., Webb, N., Esfahani, A., and Leahy, R., "Perturbation-based active flow control in overexpanded to underexpanded supersonic rectangular twin jets," *Journal of Fluid Mechanics*, Vol. 959, No. A13, 2023, pp. 1–34. https://doi.org/10.1017/jfm.2023.139.

[9] Powell, A., "The Noise of Choked Jets," *Journal of the Acoustical Society of America*, Vol. 25, No. 3, 1953, pp. 385–389. https://doi.org/10.1121/1.1907052.

[10] Edgington-Mitchell, D., "Aeroacoustic resonance and self-excitation in screeching and impinging supersonic jets — A review," *International Journal of Aeroacoustics*, Vol. 18, No. 2–3, 2019, pp. 118–188. https://doi.org/10.1177/1475472X19834521.

[11] Tam, C. K. W., and Hu, F. Q., "On the three families of instability waves of high-speed jets," *Journal of Fluid Mechanics*, Vol. 201, 1989, pp. 447–483. https://doi.org/10.1017/S002211208900100X.

[12] Jeun, J., Wu, G. J., and Lele, S. K., "Screech feedback reinforcement by coupling of twin rectangular jets," *Annual Research Briefs*, 2021, pp. 17–30.

[13] Brès, G. A., Yeung, B. C. Y., Schmidt, O. T., Esfahani, A., Webb, N., Samimy, M., and Colonius, T., "Towards large-eddy simulations of supersonic jets from twin rectangular nozzle with plasma actuation," *AIAA Paper 2021–2154*, August 2021. https://doi.org/10.2514/6.2021-2154.

[14] Brès, G. A., Bose, S. T., Ivey, C. B., Emory, M., and Ham, F., "GPU-accelerated large-eddy simulations of supersonic jets from twin rectangular nozzle," *AIAA paper 2022–3001*, June 2022. https://doi.org/10.2514/6.2022-3001.

[15] Yeung, B. C. Y., Schmidt, O. T., and Brès, G. A., "Three-Dimensional Spectral POD of Supersonic Twin-Rectangular Jet Flow," *AIAA Paper 2022–3345*, June 2022. https://doi.org/10.2514/6.2022-3345.

[16] Utkin, Y. G., Keshav, S., Kim, J.-H., Kastner, J., Adamovich, I. V., and Samimy, M., "Development and use of localized arc filament plasma actuators for high-speed flow control," *Journal of Physics D: Applied Physics*, Vol. 40, No. 3, January 2006, pp. 685–694. https://doi.org/10.1088/0022-3727/40/3/S06.

[17] Kleinman, R. R., Bodony, D. J., and Freund, J. B., "Numerical Modeling of Plasma Actuators in High Speed Jets," *AIAA paper 2009–3190*, May 2009. https://doi.org/10.2514/6.2009-3190.

[18] Kim, J., Afshari, A., Bodony, D. J., and Freund, J. B., "LES Investigation of a Mach 1.3 Jet With and Without Plasma Actuators," *AIAA Paper 2009–290*, January 2009. https://doi.org/10.2514/6.2009-290.

[19] Schmidt, O. T., "Bispectral mode decomposition of nonlinear flows," *Nonlinear Dynamics*, Vol. 102, 2020, pp. 2479–2501. https://doi.org/10.1007/s11071-020-06037-z.

[20] Nekkanti, A., Maia, I., Jordan, P., Heidt, L., Colonius, T., and Schmidt, O. T., "Triadic Nonlinear Interactions and Acoustics of Forced versus Unforced Turbulent Jets," *12th International Symposium on Turbulence and Shear Flow Phenomena*, July 2022.

[21] Schmidt, S., and Oberleithner, K., "Global modes of variable-viscosity two-phase swirling flows and their triadic resonance," *Journal of Fluid Mechanics*, Vol. 955, No. A24, 2023, pp. 1–29. https://doi.org/10.1017/jfm.2022.1079.

[22] Esfahani, A., Webb, N., and Samimy, M., "Coupling Modes in Supersonic Twin Rectangular Jets," *AIAA Paper 2021–1292*, January 2021. https://doi.org/10.2514/6.2021-1292.

[23] Brès, G. A., Ham, F. E., Nichols, J. W., and Lele, S. K., "Unstructured Large-Eddy Simulations of Supersonic Jets," *AIAA Journal*, Vol. 55, No. 4, April 2017, pp. 1164–1184. https://doi.org/10.2514/1.J055084.

[24] Sirovich, L., "Turbulence and the Dynamics of Coherent Structures Part II: Symmetries and Transformations," *Quarterly of Applied Mathematics*, Vol. 45, No. 3, 1987, pp. 573–582. https://doi.org/10.1090/qam/910463.

[25] Sirovich, L., and Park, H., "Turbulent thermal convection in a finite domain: Part I. Theory," *Physics of Fluids A*, Vol. 2, No. 9, 1990, pp. 1649–1658. https://doi.org/10.1063/1.857572.

[26] Tam, C. K. W., and Thies, A. T., "Instability of rectangular jets," *Journal of Fluid Mechanics*, Vol. 248, 1993, pp. 425–448. https://doi.org/10.1017/S0022112093000837.

[27] Rodríguez, D., Jotkar, M. R., and Gennaro, E. M., "Wavepacket models for subsonic twin jets using 3D parabolized stability equations," *Comptes Rendus Mecanique*, Vol. 346, July 2018, pp. 890–902. https://doi.org/10.1016/j.crme.2018.07.002.

[28] Esfahani, A., Webb, N., and Samimy, M., "Control of Coupling in Twin Rectangular Supersonic Jets," *AIAA Paper 2021–2122*, August 2021. https://doi.org/10.2514/6.2021-2122.

[29] Schmidt, O. T., Towne, A., Rigas, G., Colonius, T., and Brès, G. A., "Spectral analysis of jet turbulence," *Journal of Fluid Mechanics*, Vol. 855, 2018, pp. 953–982. https://doi.org/10.1017/jfm.2018.675.

[30] Tam, C. K. W., and Norum, T. D., "Impingement Tones for Large Aspect Ratio Supersonic Rectangular Jets," *AIAA Journal*, Vol. 30, No. 2, February 1992, pp. 304–311. https://doi.org/10.2514/3.10919.

[31] Welch, P. D., "The Use of Fast Fourier Transform for the Estimation of Power Spectra: A Method Based on Time Averaging Over Short, Modified Periodograms," *IEEE Transactions on Audio and Electroacoustics*, Vol. 15, No. 2, June 1967, pp. 70–73. https://doi.org/10.1109/TAU.1967.1161901.

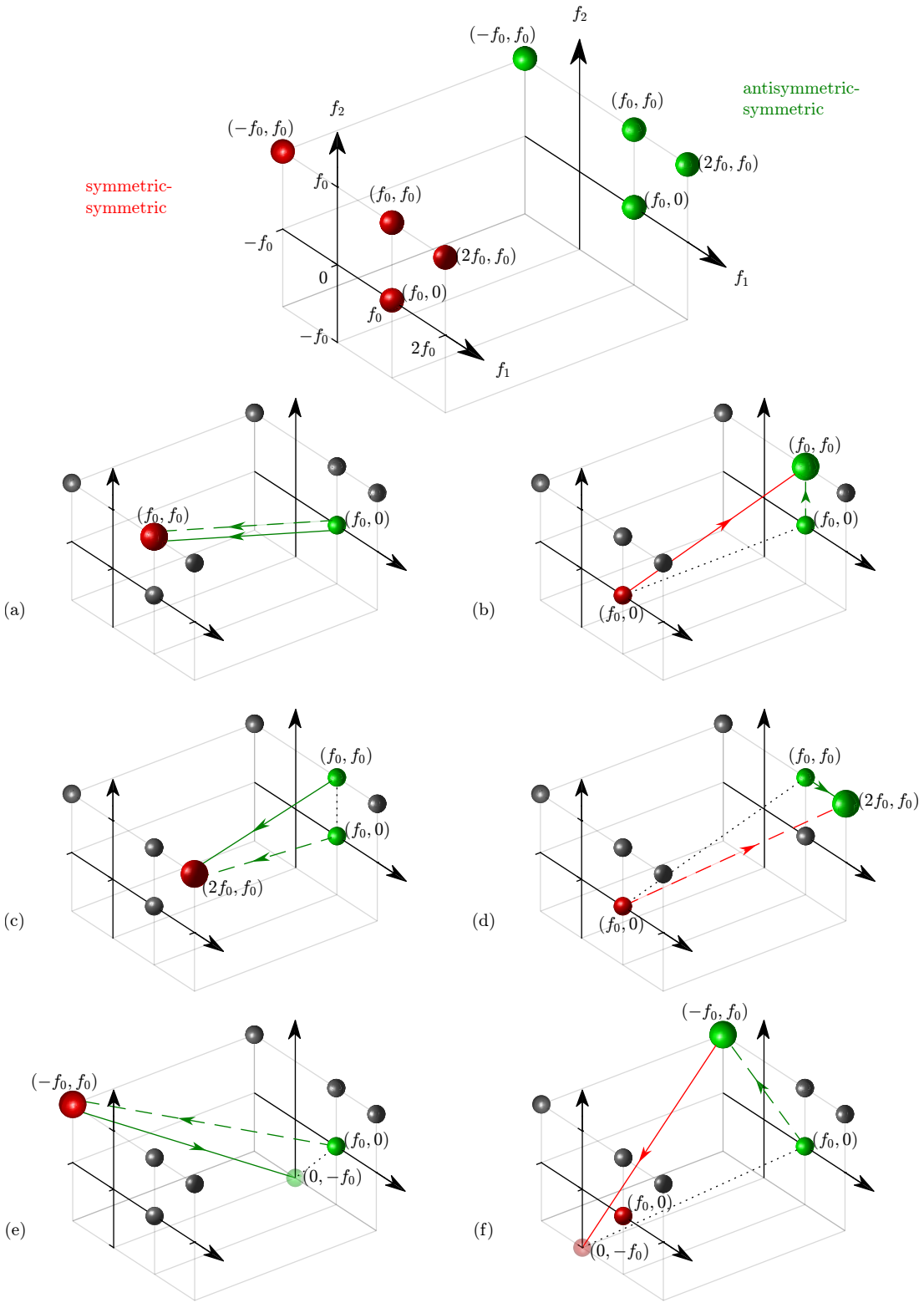

Fig. 12 Eight representative triads from the $[[\mathrm{AS}, \mathrm{AS}, \mathrm{SS}]]$ **and** $[[\mathrm{SS}, \mathrm{AS}, \mathrm{AS}]]$ **cross-bispectra in Fig. 9(b,c), reproduced at the top. Below, red (SS symmetry) and green (AS symmetry) spheres highlight the generation of the triads (a,b)** $(f_0, f_0, 2f_0)$**; (c,d)** $(2f_0, f_0, 3f_0)$**; (e,f)** $(-f_0, f_0, 0)$**, belonging to the** $[[\mathrm{AS}, \mathrm{AS}, \mathrm{SS}]]$ **(a,c,e) and** $[[\mathrm{SS}, \mathrm{AS}, \mathrm{AS}]]$ **(b,d,f) symmetry triplets. The same notation is used as in Fig. 10.**

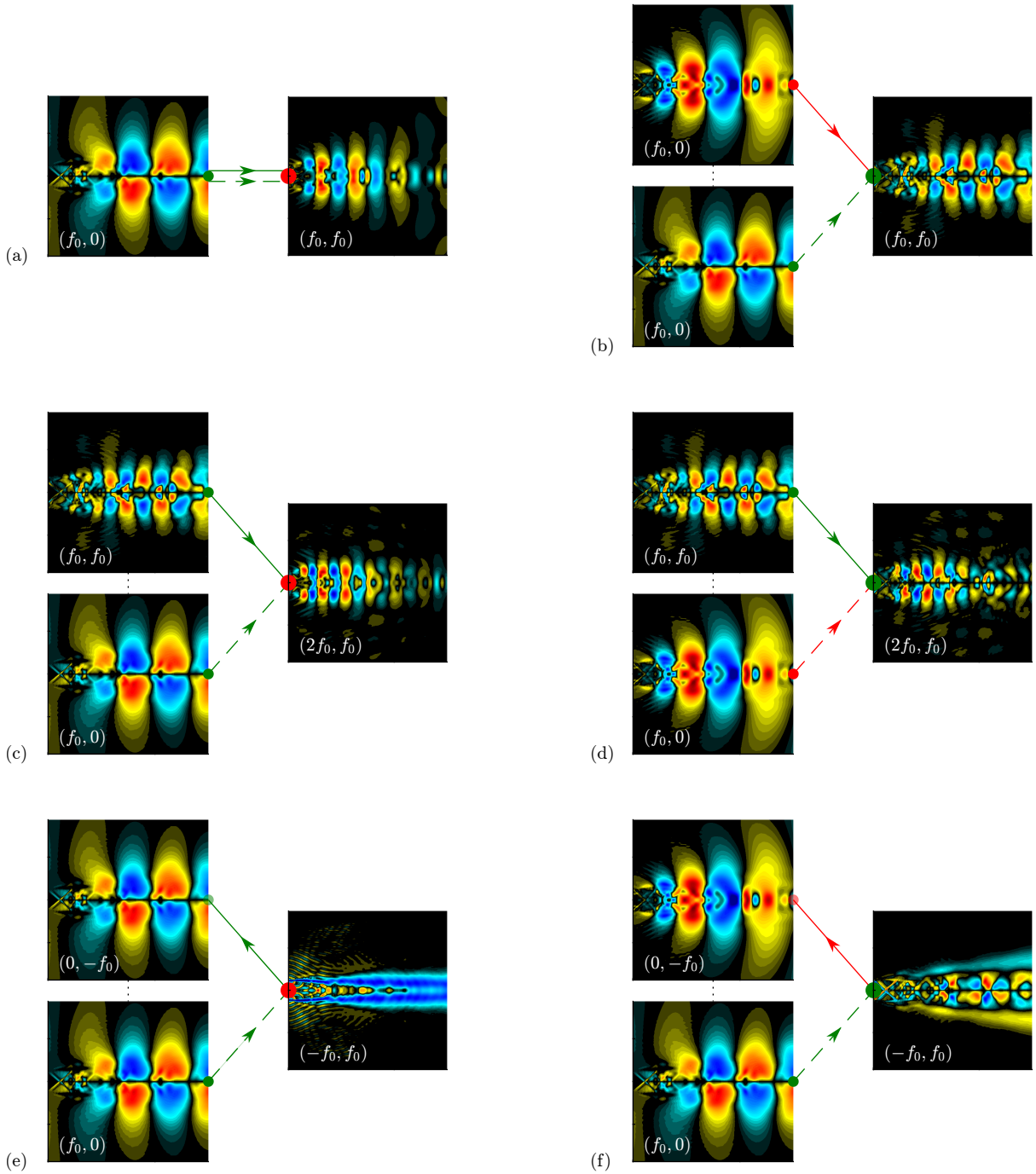

Fig. 13 Cross-bispectral modes of the [[AS, AS, SS]] and [[SS, AS, AS]] triplets, corresponding to the triads in Fig. 12. The $z = 1.8$ plane is displayed. Only the real part of each mode is shown.

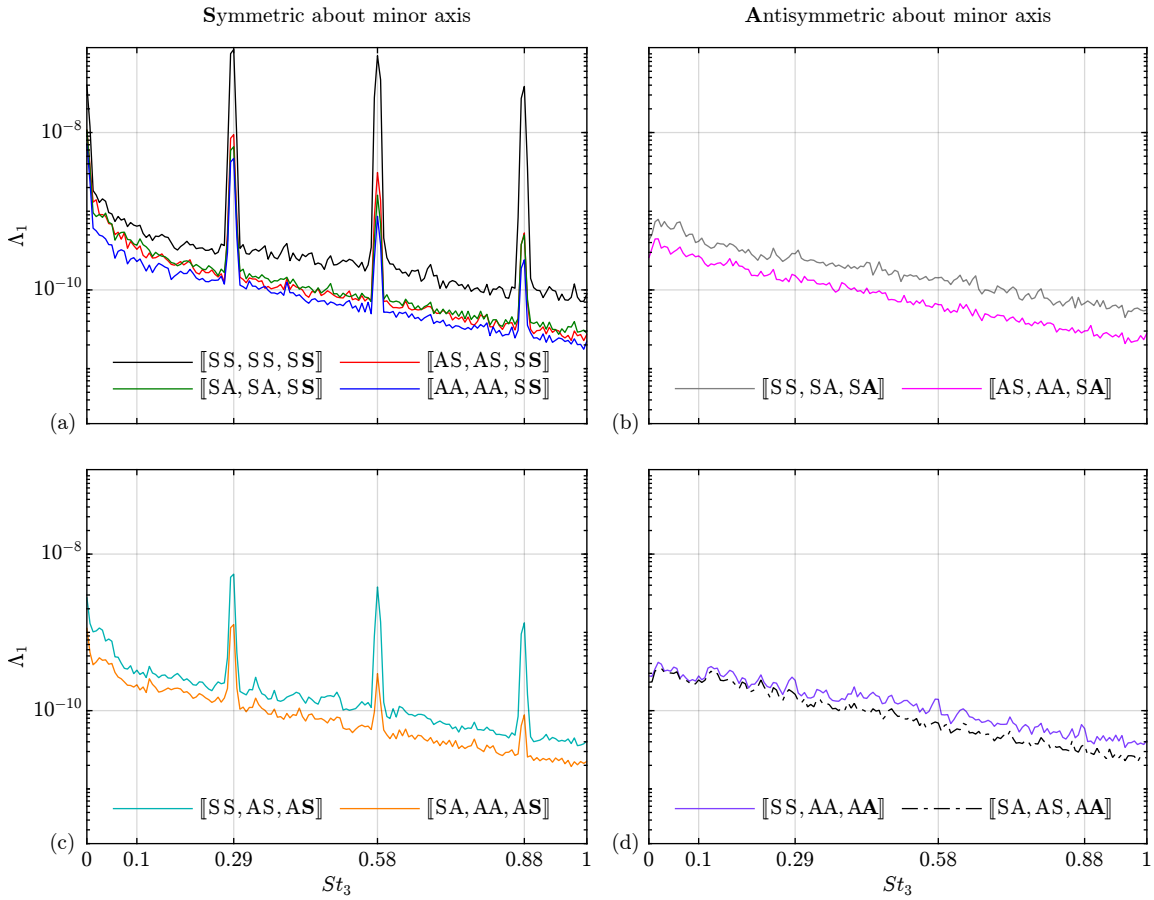

Fig. 14 BMD summed mode spectra of the forced jet. In each triplet, the mode at frequency f_{k+l} possesses: (a) SS; (b) SA; (c) AS; (d) AA symmetry. $\hat{\mathbf{q}}_{k+l}$ is symmetric (left column) or antisymmetric (right column) about the minor axis.